Nanoscale

Accepted Manuscript

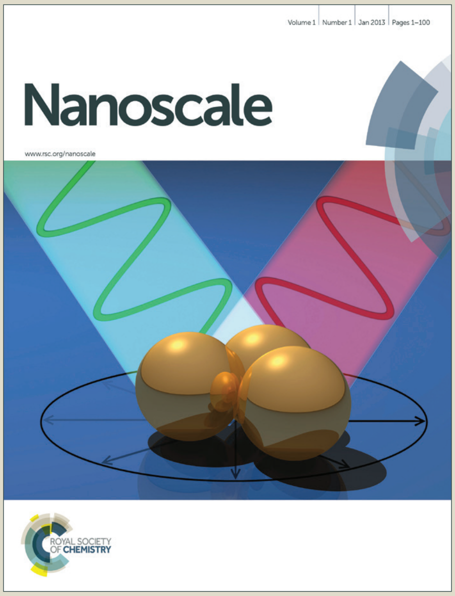

This is an *Accepted Manuscript*, which has been through the Royal Society of Chemistry peer review process and has been accepted for publication.

Accepted Manuscripts are published online shortly after acceptance, before technical editing, formatting and proof reading. Using this free service, authors can make their results available to the community, in citable form, before we publish the edited article. We will replace this *Accepted Manuscript* with the edited and formatted *Advance Article* as soon as it is available.

You can find more information about *Accepted Manuscripts* in the Information for Authors.

Please note that technical editing may introduce minor changes to the text and/or graphics, which may alter content. The journal's standard Terms & Conditions and the Ethical guidelines still apply. In no event shall the Royal Society of Chemistry be held responsible for any errors or omissions in this *Accepted Manuscript* or any consequences arising from the use of any information it contains.

ROYAL SOCIETY OF CHEMISTRY

www.rsc.org/nanoscale

Nanoscale RSCPublishing

ARTICLE

Cite this: DOI: 10.1039/x0xx00000x

Received 00th January 2012,
Accepted 00th January 2012

DOI: 10.1039/x0xx00000x

www.rsc.org/

Synthesis and characterization of Pt nanoparticles with different morphologies in mesoporous silica SBA-15 for methanol oxidation reaction

C.S. Chen[a,*], Y.T. Lai[a], T.C. Chen [b], C.H. Chen[c], J.F. Lee[d], C.W. Hsu[e], and H.M. Kao [f,*]

Mesoporous SBA-15 silica materials functionalized with and without carboxylic acid groups were used to effectively control the morphology of Pt crystals, and the materials thus obtained were applied to methanol oxidation reactions. The Pt particles aggregated to form long spheroids inside the channels in pure SBA-15. When carboxylic acid groups were utilized, the SBA-15(–COOH) material facilitated the formation of higher Pt surface area, smaller Pt nanoparticles and nearly spherical shape due to the strong interaction between Pt^{4+} ions and carboxylic acid on SBA-15. The Pt^{4+} ions on the SBA-15(–COOH) material can be directly transformed to reduced Pt particles during calcination. The methanol oxidation activity on a Pt surface is strongly dependent on shape of Pt particles. The near-spherical Pt nanoparticles on the SBA-15(-COOH) exhibited higher catalytic activity during methanol oxidation than Pt catalysts on unmodified SBA-15. The near-spherical Pt particles on the SBA-15(-COOH) contained large numbers of terrace sites on their surfaces, which led to high efficiency during methanol oxidation.

1. Introduction

Platinum catalysts have been widely used in industrial applications, including the reduction of pollutant gases in the environment, electrocatalytic reaction, hydrogenation and complete oxidation[1-13]. The enhancement of the efficiency of these Pt catalysts is important due to the high cost of Pt metal. Thus, the preparation of small metallic Pt nanoparticles (NPs) has been extensively investigated and is viewed as an active area of research in solid-state physics and chemistry. In comparison to the bulk materials, platinum NPs typically offer increased concentrations of partially coordinated surface sites, and consequently appeared to be highly reactive toward catalytic reactions. Recently, the shape- and size-controlled syntheses of Pt NPs have become an attractive goal for the development of catalysts with increased fractions of low-coordinated Pt surface atoms. In general, poly(vinyl pyrrolidone) (PVP) or poly(acrylic acid) (PAA), which are used as capping agents, can be used to prepare Pt NPs with tetrahedral, spherical, octahedral, truncated octahedral or cubic shapes.[14-19] Li and coworkers electrochemically reduced H_2PtCl_6 to prepare different morphologies of Pt NPs deposited on graphite.[7] The addition of succinic acid to the deposition solution enabled the shape of the Pt NPs to be directed toward flowerlike nanorods. The addition of thiourea and polyethylene glycol (PEG) during deposition led to isotropic Pt NP aggregates.

In recent years, mesoporous silica materials, e.g., MCM-41, MCM-48 and SBA-15, has extensively used as catalyst supports because they possess high surface areas.[20-23]

SBA-15 possesses a hexagonal arrangement of uniform channels and pore diameters that range from 5 to 30 nm, which are much larger than those of MCM-41 and MCM-48. In addition, SBA-15 exhibits a significantly lower diffusion resistance compared to those of MCM-41 and MCM-48.[22] Synthesis of copper-containing mesoporous materials has been reported in the literature.[24-26] In the preparation of Pt NPs, SBA-15 mesoporous materials are frequently used to improve the Pt dispersion and to obtain nanosized Pt particles because of their high surface areas and ordered structure.[1]

The wet impregnation method is widely used to prepare supported Pt catalysts. The growth of Pt NPs usually occurs along the direction of the channel, which results in the formation of nanowire or nanorod shapes.[1,27-32] Recently, carboxylic acid functionalized mesoporous silica materials has enabled new approaches to the synthesis of metal NPs.[33] The charged metal salts in an aqueous solution adsorb onto and

Nanoscale Accepted Manuscript

interact with the carboxylic acid groups, which are oppositely charged, in the channels of the SBA-15 support. The impregnated samples can be treated via calcination and reduction processes to form metal NPs.[33] Cu NPs could be obtained on carboxylic-acid-functionalized SBA-15 and that the prepared Cu NPs provided high dispersion at high loading and high turnover rate during the water–gas shift reaction.[34]

However, it usually attracts little attention in literatures for the formation of metal NPs on the mesoporous materials in growth mechanism and shape of NPs. In this investigation, we used the SBA-15 materials with and without carboxylic acid groups (–COOH) as supports to control the different morphologies of Pt NPs in the channels of SBA-15 materials. The catalytic activity of methanol oxidation reaction was compared on the different morphologies of Pt NPs. We used a variety of experimental techniques to characterize the Pt NPs and to probe the mechanism of formation of the Pt NPs.

2. Experimental

2.1 Preparation of Pt NPs

The –COOH-functionalized mesoporous silica SBA-15 was synthesized according to our previously reported method.[34] In a typical synthesis, the triblock copolymer Pluronic P123 (1.00 g) was dissolved in 31.25 g of 1.9 M HCl, and the mixture was continuously stirred for 4 h at 313 K. Tetraethoxysilane (TEOS, from Aldrich) and carboxyethylsilanetriol (CES, 25 wt.% in water from Gelest) was pre-mixed, and then added dropwise to the solution with vigorous stirring. The solution was allowed to react for 20 h at 313 K. Afterward, the milky mixture was under hydrothermal treatment at 373 K for 24 h. The molar composition of the reaction mixture was 0.1 CES: 0.9 TEOS: 0.0168 P123: 5.85 HCl: 162.68 H_2O. The resultant precipitate was collected via filtration, washed with water and air-dried at room temperature. The template P123 was removed from the as-synthesized materials (0.6 g) by adding H_2SO_4 (100 g, 48 wt.%) and heating the mixture at 368 K for 24 h. The product was washed with water and dried at 363 K and was denoted as SBA-15(-COOH). The 2.52 % and 0.85 % Pt/SBA-15(-COOH) catalysts were prepared by impregnating SBA-15(-COOH) with 20 mL of 10 % and 2% aqueous H_2PtCl_6 solutions. The as-impregnated Pt^{4+}/SBA-15(-COOH) solid was collected via filtration and subsequently air-dried at 353 K for 10 h. The 2.48 % and 0.87 % Pt/SBA-15 catalysts were prepared by impregnating SBA-15 with 20 mL of an aqueous solution of H_2PtCl_6, respectively. Samples of Pt^{4+} impregnated on SBA-15 were directly dried in air at 353 K for 10 h. All Pt catalysts were calcined in air and reduced under H_2 at 673 K for 5 h prior to use in methanol oxidation reactions.

2.2 In situ X-ray absorption spectroscopy (XAS)

XAS spectra were recorded at the BL17C1 beam line at the National Synchrotron Radiation Research Center (NSRRC), Taiwan, with an electron storage ring operated at 1.5 GeV. All of the XAS powder studies of the NPs were conducted in a custom stainless steel cell. Two holes were made in the cell: one on the top of the cell and the other on one side. After the solid samples were placed inside the cell, the holes were closed with Kapton film to avoid exposure of the sample to the ambient atmosphere. All spectra were recorded at room temperature in transmission mode. The higher harmonics were eliminated via detuning of the double Si (111) crystal monochromator. Three gas-filled ionization chambers were used in series to measure the intensities of the incident beam (I_0), the beam transmitted by the sample (I_t) and the beam subsequently transmitted by the reference foil (I_r). The third ion chamber was used in conjunction with the Pt foil reference sample for the Pt L_3-edge measurements. The parameters for the extended X-ray absorption fine structure (EXAFS) measurements, data collection modes and error calculations were all controlled according to the guidelines set by the International XAFS Society Standards and Criteria Committee. The EXAFS data were reduced using standard procedures. We obtained the EXAFS function χ by subtracting the post-edge background from the overall absorption and normalizing with respect to the edge jump step. The normalized $\chi(E)$ was transformed from energy space to k-space, where k is the photoelectron wave vector. The $\chi(k)$ data were multiplied by k^2 for the Pt L_3-edge experiments to compensate for the dampening of the EXAFS oscillations in the high k region. Subsequently, the $\chi(k)$ data in k-space, which ranged from 3.1 to 12.4 $Å^{-1}$ for the Pt L_3-edge, were Fourier transformed (FT) to r-space to separate the EXAFS contributions from the different coordination shells. All computer programs were implemented using the UWXAFS 3.0 software package, and the backscattering amplitude and the phase shift for the specific atom pairs were theoretically calculated using the FEFF7 code. From these analyses, structural parameters such as the coordination number (N) and the bond distance (R) were successfully calculated.

2.3 Catalytic tests for methanol oxidation

All methanol oxidation reactions were performed in a fixed-bed reactor (0.95 cm inner diameter) at atmospheric pressure. A thermocouple connected to a PID temperature controller was placed atop the catalyst bed. The reactions were performed using an air stream with a total flow rate of 30 mL/min passing through liquid methanol at 263 K, and the resulting mixture of O_2/MeOH in a 9.8:1 molar ratio was passed over 1 mg of catalyst diluted with 200 mg SiO_2. The conversion of the reaction was maintained below 10% to ensure that the conditions were similar to differential conditions. All products were analyzed via gas chromatography (GC) through a 12-ft Porapak-Q column; the gas chromatograph was equipped with a thermal conductivity detector (TCD). The turnover frequency (TOF) was calculated using the formula: TOF=[conversion×0.01 (mL/s for MeOH)×6.02 $\times 10^{23}$ (molecules/mol)]/[24400 (mL/mol)×Pt sites].

2.4 Transmission electron microscopy (TEM)

Nanoscale Accepted Manuscript

This journal is © The Royal Society of Chemistry 2012

High-resolution TEM analyses were performed on a JeJEOL-JEM3000F instrument located at the High Valued Instrument Center of the National Tsing Hua University, Taiwan. The instrument was operated at 300 keV. After the catalyst samples were pre-treated, they were dispersed in methanol, and the solution was ultrasonically mixed at room temperature. A portion of this solution was dropped onto a Cu grid for TEM imaging.

2.5 Temperature-programmed desorption (TPD)

TPD experiments were performed in a 100-mL/min stream of He at atmospheric pressure in a conventional flow system. The temperature was increased from 300 to 1000 K at a rate of 10 K/min over the course of the TPD process. All of the signals were measured with a VG Smart IQ+ 300D mass spectrometer. The temperature was measured with a K-type thermocouple, which was inserted into the catalyst bed, and the desorbed products were admitted into the vacuum chamber through a leak valve using He as the carrier gas. The operating pressure in the chamber was approximately 3×10^{-7} Torr, and the base pressure in the chamber was approximately 2×10^{-9} Torr.

2.6 Measurement of the platinum surface area

The Pt contents of the Pt/SBA-15 and Pt/SBA-15(-COOH) samples were measured by inductively coupled plasma mass spectrometry (ICP/MS), which was performed at the High Valued Instrument Center of the National Sun Yat-sen University, Taiwan. The Pt surface areas of the Pt/SBA-15 and Pt/SBA-15(-COOH) samples were measured via saturated CO chemisorption at room temperature in a vacuum system. The average surface density for the Pt metal was 7.1×10^{18} Pt atoms/m^2.

2.7 Measurement of the FT-IR spectra

The in situ DRIFT analysis of the CO and methanol adsorption was performed with a Nicolet 5700 FTIR spectrometer equipped with a mercury cadmium telluride (MCT) detector; the instrument was operated at a 1 cm^{-1} resolution over 256 scans. The DRIFT cell (Harrick) was equipped with ZnSe windows and a heating cartridge that allowed the sample to be heated to 773 K. We induced the adsorption of methanol by injecting a 5 μL liquid sample onto the Pt/SBA-15 catalysts. The IR spectra of the CO adsorption on Pt/SBA-15 was obtained using pure CO that was passed through Pt/SBA-15 samples for 30 min at room temperature; the residual gaseous CO was purged for 60 min. Methanol was dosed onto all catalysts by injection with a 10 μL Hamilton 7001 syringe through a port located at the upstream of the DRIFT cell. The injection port, which was similar to that used in gas chromatography, was heated to 373 K to prevent the condensation of methanol

3. Results

3.1 Characterization of the Pt/SBA-15 and Pt/SBA-15(-COOH).

Figure 1A shows the small-angle XRD patterns of the SBA-15(-COOH) and SBA-15 supports both with and without the reduced Pt NPs. Each spectrum exhibited three well-resolved diffraction peaks in the region of 2θ=0.5–2.0°, which were indexed to the (100), (110) and (200) diffractions that are characteristic of mesoporous silica materials with *p6mm* hexagonal symmetry. The carboxylic-acid-functionalized SBA-15 exhibited a weaker and broader d_{100} peak, which indicated the partial degradation of the ordered pore structure of the SBA-15. The formation of reduced Pt particles may cause a shift in the diffraction peaks toward higher angles relative to the peaks of the SBA-15(-COOH) and SBA-15 supports due to a contraction of the framework accompanied by a decrease in the cell parameter a_0. It implied that formation of Pt NPs might be confined in the channels of SBA-15. Figure 1B shows the X-ray diffraction (XRD) patterns of the face-centered cubic (fcc) Pt structures on the SBA-15 and SBA-15(-COOH), which exhibited peaks at 2θ= 39.6°, 46.0°, 67.2°, 81.0° and 85.3°; these peaks correspond to the (111), (200), (220), (311) and (222) facets, respectively. Figure 2 displays the N_2 adsorption–desorption isotherms of the mesoporous silica materials both with and without Pt particles. All of the samples exhibited type IV adsorption isotherms. A H2-type hysteresis was observed, which suggested that the mesoporous channels changed from cylindrical to ink-bottle-shaped because the Pt particles partially blocked the pores.

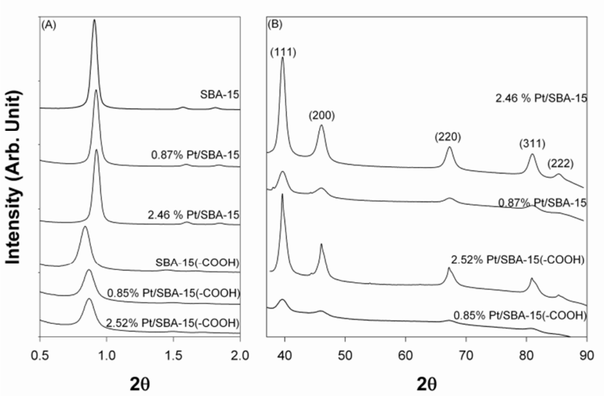

Figure 1 (A) Small-angle XRD patterns for the Pt/SBA-15 and SBA-15 samples without and with –COOH functional groups; (B) wide-angle XRD spectra for all of the Pt/SBA-15 and Pt/SBA-15(-COOH) catalysts.

Nanoscale Accepted Manuscript

Table 2 Characterization of Pt/SBA-15 (-COOH) and Pt/SBA15 catalysts

Catalyst	CO adsorption[a] (μmol/g cat.)	Pt surface area[a] (m^2/g)	Pt particle size[b] (nm)
0.85% Pt/SBA-15 (-COOH)	1.96	0.18	5.4
2.52% Pt/SBA-15 (-COOH)	4.76	0.44	7.6
0.87% Pt/SBA-15	1.16	0.11	5.9
2.46% Pt/SBA-15	3.84	0.35	8.8

[a] The amount of CO adsorption and Pt surface areas of the Pt/SBA-15 and Pt/SBA-15(-COOH) samples were measured via saturated CO chemisorption at room temperature in a vacuum system. [b] The average particle size of all the reduced Pt NPs were calculated from the Pt(111) pattern of XRD spectra according to the Scherrer equation using the full-width at half maximum (fwhm) values.

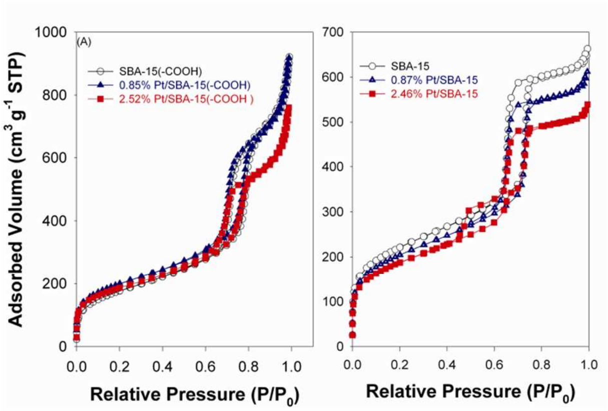

Figure 2 N_2 adsorption–desorption measurements for (A) the SBA-15(-COOH) and Pt/SBA-15(-COOH) samples; (B) SBA-15 and Pt/SBA-15 samples.

The pore size distributions of the samples, which were calculated from the N_2 adsorption isotherms according to the Barrett–Joyner–Halenda (BJH) method with calibration, are provided in Figure S1. The pore size of the SBA-15(-COOH), both with and without the Pt particles, was slightly larger than those of the SBA-15 and Pt/SBA-15 and were centered at 7.3 nm. The samples contained few micropores (< 0.006 cm^3/g). The textural properties that were obtained from the N_2 adsorption–desorption measurements are summarized in Table 1. In Table 2, the parameters of the reduced Pt particles on the SBA-15 material are compared to those of the Pt particles on the SBA-15(-COOH) material. This comparison includes the quantity of CO adsorbed, the Pt surface area and the Pt particle size. The average particle size of all the reduced Pt/SBA-15 samples was calculated from the Pt(111) peak according to the Scherrer equation using the full-width at half maximum (fwhm) values. It can be observed that Pt NPs deposited on SBA-15(-COOH) could cause higher Pt surface area and smaller particle size than that on SBA-15.

Table1. Textural properties of the SBA-15 and SBA-15(-COOH) with and without Pt NPs

Sample	2θ	d_{100} (nm)	a_0 (nm)	V (cm^3/g)	D (nm)	S_{BET} (m^2/g)
SBA-15	0.91	9.7	11.21	1.0	6.2	759
0.87% Pt/SBA-15	0.92	9.6	11.08	0.9	6.2	702
2.46% Pt/SBA-15	0.93	9.5	10.97	0.9	6.2	692
SBA-15(-COOH)	0.84	10.5	12.14	1.4	7.3	689
0.85% Pt/ SBA-15(-COOH)	0.87	10.2	11.72	1.4	7.3	641
2.52% Pt/ SBA-15(-COOH)	0.87	10.2	11.72	1.2	7.3	624

a_0: cell parameter; V: pore volume; D: pore diameter; S_{BET} was calculated according to the Brunauer–Emmett–Teller (BET) method in the relative pressure range of $p/p_0 = 0.05–0.3$; D was analyzed by the desorption branch of the isotherms by the Barrett–Joyner–Halenda (BJH) method; V was obtained from the volumes of N_2 adsorbed at $p/p_0 = 0.95$ or in the vicinity.

The high-resolution TEM result of calcined Pt NPs formed on SBA-15 was shown in Figure S2. It can see that Pt^{4+} ions could apparently aggregate to form long rod-like Pt NPs inside the channels of SBA-15 through calcined at 673 K for 5 h. Figure 3 shows the typical TEM images for the Pt NPs on the SBA-15 material. A large amount of long, spheroidal Pt NPs were formed inside the channels of the pure SBA-15 structure (images a and b), after calcined Pt NPs were reduced in H_2 at 673 K for 5 h. The crystalline structure of the side view of reduced Pt NPs on SBA-15 has been further analyzed with HRTEM and fast Fourier transform (FFT) images to obtain clear lattice images of the Pt structure, which was shown in image c. The spheroid-like Pt NPs are covered by the (111) and (200) facets. The lattice fringe measurements with an interplanar spacing of 0.227 nm and 0.196 nm were assigned to the (111) and (200) facets. The long spheroid Pt NPs possessed a twin plane running through the middle along the long axis. The FFT pattern that was obtained from an individual Pt NP with the simulated electron beam along the direction of the [-110] zone axis revealed a twin plane parallel to the growth direction of the NPs. The high-resolution TEM images in Figures 3d and 3e show the top view of the spheroid-like Pt NP. The boundary of the single Pt NP was assigned to the (200) facet. The FFT pattern was obtained from the Pt NP with the simulated electron beam along the direction of the [101] zone axis. The top plane of the Pt NP could contain five-fold single-crystal surfaces and gave a complex FFT pattern (top-left image). Most of the images indicate four-fold twinned structures, possibly because the twinned boundaries may not be focused at the same level along the non-axial direction. The top plane of the Pt NP was composed of five (111) single-crystals and the five-fold twinned structures are bounded by {111} facets. In this work, the HRTEM images of Pt NPs outside the channels of SBA-15 showed that the NPs simultaneously exhibited both cubic and rhombic shapes, as shown in Figures 3f and 3g. We proposed that the Pt NPs with preferential octahedral shapes formed on the pure SBA-15 support.

Nanoscale Accepted Manuscript

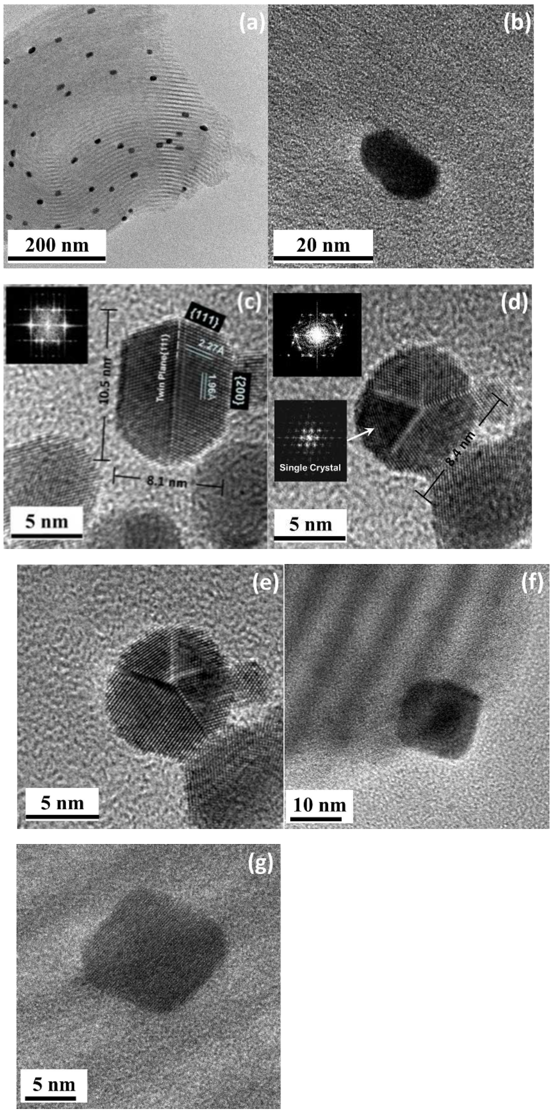

Figure 3 high-resolution TEM images of reduced 2.46% Pt NPs on SBA-15

Figure 4 reveals the high-resolution TEM images for reduced Pt NPs deposited on SBA-15(-COOH). However, the same calcination treatment in air at 673 K for 5 h can induce the near-spherical Pt NPs formed on the SBA-15(-COOH), as shown in Figure S2. Notably, a large number of near-spherical Pt NPs were still generated on the SBA-15(-COOH) through reduction treatment, as shown in Figure 4a. It could be observed that the near-spherical Pt NPs might form inside the channels of SBA-15 and/or on support surface. Figure 4b reveals the high-resolution TEM image of a single Pt NP and demonstrates that the particle was bounded by a mix of both (200) and (220) facets. The lattices fringes at 0.201 nm and 0.139 nm were consistent with the (200) and (220) lattice spacing of fcc Pt. Furthermore, the facets of the NPs were identified through indexing of the FFT pattern, which implies that the Pt particle is a single crystal bounded by a mix of both {200} and {220} facets. The TEM results of ca. 0.9 % Pt NPs deposited on SBA-15 and SBA-15(-COOH) are shown in Figure S3. It was also observed that the rod-shaped Pt NPs and near-spherical Pt NPs could form on SBA-15 and SBA-15(-COOH) supports, respectively.

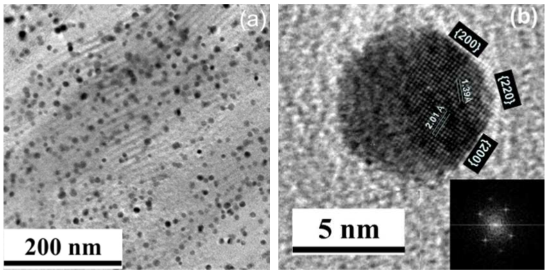

Figure 4 high-resolution TEM images of reduced 2.52% Pt NPs on SBA-15(-COOH)

3.2 X-ray absorption spectroscopy (XAS)

Figure 5 shows the L_3-edge X-ray absorption near edge structure (XANES) spectra of the Pt while undergoing various pretreatments on the SBA-15 and SBA-15(-COOH) supports. The white line representing the resonance peak at the absorption edge can be attributed to the electron transition from $2p_{3/2}$ to $5d_{5/2}$ and $5d_{3/2}$.[2-4,35,36] The intensity of the white line at the L_3 edge indicates the electronic state of the absorbing atoms. A more intense white line implies a greater electron vacancy in the d-orbitals.[2-4,35,36] For the Pt/SBA-15 sample, the intensity of the white line for the Pt^{4+}-impregnated SBA-15 decreased with continued calcination and reduction pretreatments, which agrees with the transformation of Pt^{4+} to Pt^0 (Figure 5A). Furthermore, the intensity of the white line for the calcined Pt/SBA-15 sample was substantially greater than that of the reduced Pt/SBA-15. Interestingly, the white lines for the Pt^{4+} species on SBA-15(–COOH) after calcination at 673 K for 5 h were lightly more intense than that of the reduced Pt/SBA-15(–COOH) (Figure 5B). The local structures of the Pt atoms in the Pt/SBA-15 and Pt/SBA-15(-COOH) catalysts were investigated via L-edge extended X-ray absorption fine structure (EXAFS) with Pt foil as a reference material. The FT k^2-weighted EXAFS results at the Pt L-edge with phase correlation for the impregnated, calcined and reduced Pt loading on the SBA-15 and Pt/SBA-15(-COOH) supports are shown in Figure 6. The $k^2x(k)$ spectra were obtained through a comparison of the FEFF theoretical fit with the back-transformed experimental EXAFS data. The structural parameters of the calcined and reduced Pt samples that were extracted from the best-fit EXAFS data are listed in Table 3. The calcined Pt on pure SBA-15 was analyzed to obtain the Pt–O and Pt–Pt bonding information: 2.14 Å for the Pt–O bonding and 2.79 Å for the Pt–Pt bonding. Coordination numbers of 2.9 and 4.1 were obtained for the Pt–O and Pt–Pt bonding, respectively. When carboxylic acid groups were present on the SBA-15, the calcination treatment led to a strong reduction of Pt^{4+} species, which formed metallic Pt particles in air. The coordination number $N_{Pt\text{-}O}$ was approximately 0.2. The bond distance of 2.77 Å for the Pt–Pt bond was nearly identical to

Nanoscale Accepted Manuscript

that observed for the coordination environments of the metallic Pt species.

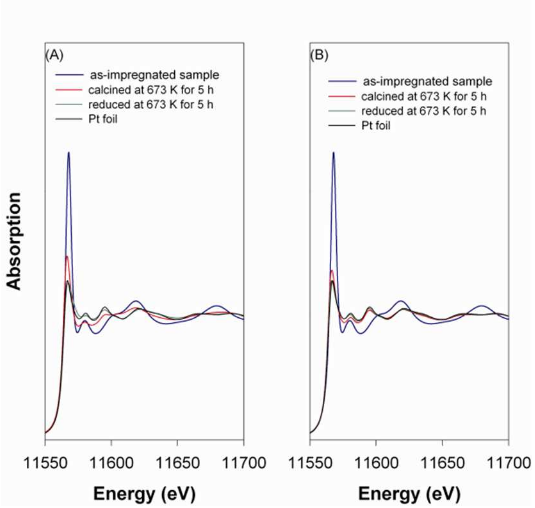

Figure 5 Pt L-edge XANES spectra of the impregnated, calcined and reduced Pt samples for (A) 2.46% Pt/SBA-15 and (B) 2.52% Pt/SBA-15(-COOH).

2.46% Pt/SBA-15	Shell	N	R (Å)	r^a ($\times10^{-2}$)	σ^2 ($Å^2$)^b	ΔE_0 (eV)^c
impregnation	Pt–Cl	5.5	2.30	1.90	0.0026	10.0
calcination	Pt–O	2.9	2.14	3.41	0.0080	16.5
	Pt–Pt	4.1	2.79	3.41	0.0049	14.2
reduction	Pt–Pt	7.9	2.77	0.34	0.0064	7.0
2.52%Pt/SBA-15 (-COOH)						
impregnation	Pt–Cl	5.8	2.32	1.76	0.0060	8.0
calcination	Pt–O	0.2	2.06	0.10	0.0010	12.7
	Pt–Pt	8.2	2.77	0.10	0.0054	7.6
reduction	Pt–Pt	9.2	2.77	0.14	0.0050	7.0

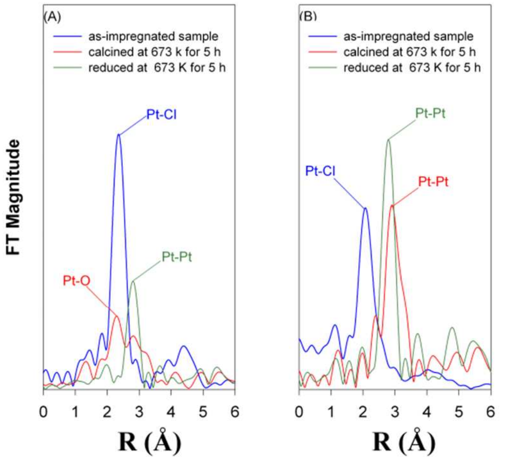

Figure 6 Fourier-transformed EXAFS spectra for the impregnated, calcined and reduced Pt samples of (A) 2.46 % Pt/SBA-15 and (B) 2.52% Pt/SBA-15(-COOH).

Table 3 Structural parameters of impregnated, calcined and reduced Pt on SBA-15 and SBA-15(-COOH).

^{a}Residual factor; ^{b}Debye－Waller factor, ^{c}The inner potential correction

Figure 7A shows the temperature-dependent in situ L_3-edge XANES spectra of Pt^{4+} species on SBA-15(–COOH) at 298-673 K in an air stream. The spectrum of the impregnated Pt^{4+}/SBA-15(-COOH) showed a greater white line intensity because of its strongly oxidized character. The white line for the Pt species was slightly decreased in intensity from 298 to 623 K; it was significantly diminished as the temperature was increased to 673 K. The corresponding FT k^2-weighted EXAFS and curve-fitting results are shown in Figure 7B and Table 4. The fitting results indicated that the impregnated Pt^{4+}/SBA-15(-COOH) at 298 K appeared to have Pt–Cl coordination. We observed that the coordination number of $N_{Pt\text{-}Cl}$ gradually decreased with increasing temperature. When the calcination temperature was increased to 623 K, the partial Pt–Pt bonding was demonstrated to have a low coordination number of 1.3. As the calcination temperature was increased to 673 K, the character of Pt species was apparently shifted toward metallic Pt and weak Pt–O bonding. The XANES spectra of Pt^{4+}/SBA-15(-COOH) in a N_2 stream at different temperatures were compared in Figure 7C, which revealed that the white line intensity also decreased when the temperature was increased. The EXAFS results for the Pt^{4+}/SBA-15(–COOH) subjected to a thermal treatment in a N_2 stream at 673 K are listed in Table 4. The results show the formation of fully reduced Pt metal with a bond distance of 2.78 Å and a coordination number $N_{Pt\text{-}Pt}$ of 9.7 for Pt–Pt bonding. These results suggest that the Pt^{4+} ions on SBA-15(–COOH) could be directly transformed to reduced Pt particles during thermal treatment at 673 K. The formation of the weak Pt–O bonding in air at 673 K might be due to the reduced Pt particles becoming slightly oxidized by air at high temperatures.

Nanoscale Accepted Manuscript

This journal is © The Royal Society of Chemistry 2012

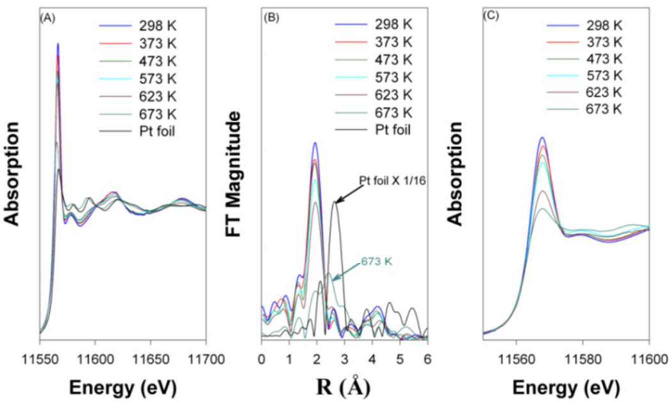

Fig. 7 (A) in-situ Pt L_3-edge XANES spectra and (B) Fourier-transformed EXAFS spectra of Pt^{4+}/SBA-15(-COOH) in an air stream at different temperatures; (C) in-situ Pt L_3-edge XANES spectra of Pt^{4+}/SBA-15(-COOH) in a N_2 stream at different temperatures.

3.3 In situ XRD spectroscopy

The *in-situ* XRD spectra of the impregnated Pt^{4+}/SBA-15 and Pt^{4+}/SBA-15(-COOH) were used to further probe the transformation of Pt species during calcination, as shown in Figure 8. The diffraction patterns are identified using the JCPDS database. In Figure 8A, several diffraction patterns regarding the formation of $(H_3O_2)PtCl_6$ crystal could be observed in the Pt^{4+}/SBA-15 samples at room temperature. The characteristic peaks for the $(H_3O_2)PtCl_6$ species gradually vanished with increasing temperature and transformed into PCl_2 species peaks at 513 K. The complicated diffraction peaks of PCl_2 species could rapidly disappear at temperature greater than 573 K, and exhibited new peaks at 39.6°, 46.0°, 67.2°, 81.0° and 85.3°. These five diffraction peaks for Pt species at 673 K can likely associate with Pt_2O or metallic Pt crystals resulting from the search in JCPDS database. However, the EXAFS results in Table 3 have indicated that Pt-O bonding could be formed on the Pt^{4+}/SBA-15 undergoing calcination treatment. Thus, it provided the likelihood of that Pt_2O might be the major species of Pt^{4+}/SBA-15 after calcination. Figure 8B shows the *in-situ* XRD spectra of the Pt^{4+}/SBA-15(-COOH) calcined in air as a function of temperature. No obvious diffraction peaks of $(H_3O_2)PtCl_6$ crystal was observed during Pt^{4+} impregnated on SBA-15(-COOH), indicating that the strong interaction between Pt^{4+} ions and carboxylic acid on SBA-15 might occur. The diffraction peaks at 39.6°, 46.0°, 67.2°, 81.0° and 85.3° were also observed in the spectra at or above the calcination temperature of 573 K. The emergence of these diffraction peaks was attributed to metallic Pt particles on SBA-15(-COOH), because the EXAFS results in Table 4 had demonstrated that Pt^{4+} species could be directly transformed to metallic Pt NPs on SBA-15(-COOH) in an air environment.

Table 4 Temperature-dependent structural parameters of Pt^{4+} impregnated on SBA-15(-COOH)

Temperature (K)	Shell	N	R (Å)	r^a ($\times 10^{-2}$)	σ^2 ($Å^2$)^b	ΔE_0 (eV)^c
298 (air)	Pt–Cl	5.8	2.32	1.76	0.006	8.0
373 (air)	Pt–Cl	5.3	2.32	0.94	0.006	9.7
473 (air)	Pt–Cl	5.2	2.32	0.67	0.005	9.0
523 (air)	Pt–Cl	4.3	2.33	1.10	0.004	9.5
573 (air)	Pt–Cl	4.6	2.33	0.40	0.006	9.8
623 (air)	Pt–Cl	3.5	2.34	0.50	0.005	9.7
	Pt–Pt	1.3	2.80	0.50	0.006	5.0
673 (air)	Pt–O	0.6	2.19	0.72	0.001	9.9
	Pt–Pt	9.4	2.80	0.72	0.011	9.5
673 (N_2)^d	Pt–Pt	9.7	2.78	0.21	0.015	7.5

[a] Residual factor; [b] Debye—Waller factor, [c] The inner potential correction, [d] calcination in N_2 at 673 K for 5 h

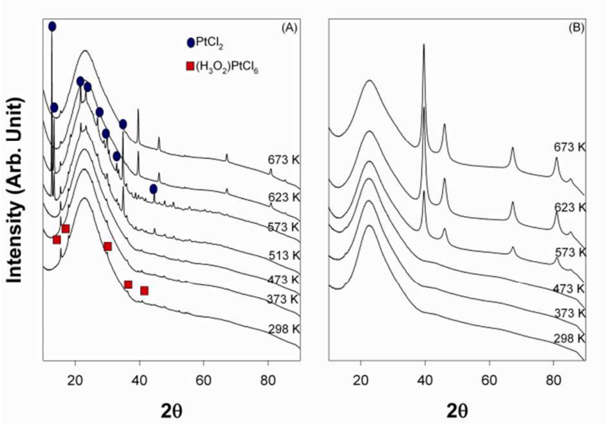

Figure 8 In-situ XRD spectra of (A) impregnated Pt^{4+}/SBA-15 and (B) Pt^{4+}/SBA-15(-COOH) in air at various calcination temperatures.

3.3 Catalytic methanol oxidation over the Pt/SBA-15 and Pt/SBA-15(-COOH) catalysts.

The dependence of the specific turnover frequency (TOF) as a function of temperature for the Pt/SBA-15 and Pt/SBA-15(-COOH) catalysts is shown in Figure 9. It can find that the Pt/SBA-15(-COOH) exhibited dramatically higher methanol oxidation activity compared to the Pt/SBA-15. The TOF for methanol oxidation increased in the following order: 2.5 % Pt/SBA-15 < 0.9 % Pt/SBA-15 < 2.5 % Pt/SBA-15(-COOH) < 0.9 % Pt/SBA-15(-COOH).

Nanoscale Accepted Manuscript

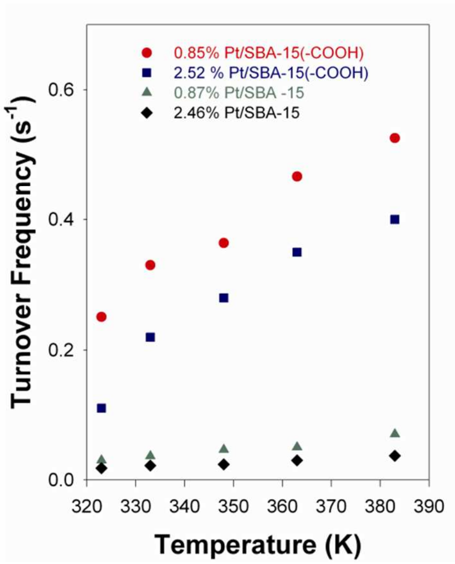

Figure 9 Comparison of the turnover frequency in methanol oxidation between the Pt/SBA-15 andPt/SBA-15(-COOH) catalysts for the temperature-dependent reactions.

The large difference in activity of methanol for Pt/SBA-15(-COOH) and Pt/SB-15 catalysts were considered to associate with the distribution of active site on different surface of Pt NPs. We used CO as a probe molecule to identify the active sites on the reduced Pt catalysts due to its utility with vibrational spectroscopy, which can provide information related to the surface sites of an adsorbed species and the chemical environment of a Pt surface. The difference between the CO adsorbed on the reduced Pt/SBA-15 with and without –COOH groups was specifically examined in this work. Figure 10 shows the IR spectra of the CO adsorbed on both of the Pt/SBA-15 catalysts at room temperature. The IR peak at 1831 cm^{-1} was attributed to a bridge-type CO adsorption on both of the Pt/SBA-15 catalysts. The vibrational frequency of the IR bands at frequencies greater than 2000 cm^{-1} was assigned to a linear CO adsorption on the Pt surfaces. The IR spectrum of the CO adsorbed on Pt/SBA-15 was fitted with two principal peaks at 2050 cm^{-1} (L_1 state) and 2076 cm^{-1} (L_2 state). A new CO adsorption peak at 2094 cm^{-1} (L_3 state) appeared in the spectrum of the Pt/SBA-15(–COOH) surface.

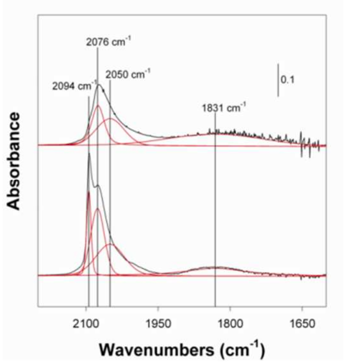

Fig. 10 IR spectra of the CO adsorbed onto the reduced 2.46% Pt/SBA-15 and 2.52% Pt/SBA-15(-COOH) at 298 K.

Figure 11A presents the IR spectra for the methanol oxidation over Pt/SBA-15(-COOH) under flowing air at 298 K. Initially, the methanol that was adsorbed onto the Pt/SBA-15(-COOH) was strongly dissociated at room temperature; therefore, the IR bands for the linear CO adsorption and ν(C=O) of the carbonyl species at 1710 cm^{-1} formed rapidly. The peaks for ν(C-H) appeared at 2848, 2919, 2954 and 3001 cm^{-1}. An enlarged view of the spectrum associated with CO adsorption is provided in Figure 11B, which demonstrates that the IR peaks were primarily positioned at 2051 cm^{-1} (L_1 CO) and 2074 cm^{-1} (L_2 CO). The adsorbed CO that was derived from the methanol dissociation was completely consumed by the air to generate CO_2 within 3 min. The other ν(C-H) signals also disappeared as the oxidation reaction progressed. However, the peak of the carbonyl species at 1710 cm^{-1} maintained a constant intensity throughout the oxidation process. The peak at 1622 cm^{-1} was attributed to the bending mode of the H_2O adsorbed during the methanol oxidation. The IR spectra of the methanol that was adsorbed onto the Pt/SBA-15 in air are shown in Figure S4. The ν(CO) of the carbonyl species was observed at 1710 cm^{-1}; however, the peak of the adsorbed CO appeared primarily at 2052 cm^{-1} due to the dissociation of the methanol. The intensity of the IR bands for all of the adsorbed species did not change significantly when air was flowed over the Pt surface that was already covered with methanol for 30 min. No evident IR peak was generated for the adsorbed H_2O at 1622 cm^{-1}, which indicated poor methanol oxidation efficiency over this Pt surface.

Therefore, the sites for methanol dissociation were further identified using the IR spectra of the methanol and CO that were co-adsorbed onto the Pt/SBA-15 and Pt/SBA-15(-COOH) catalysts. The adsorbed methanol molecules exhibited no clear decomposition on the Pt/SBA-15(-COOH) surface (Figure 12A) when the Pt surface was pre-saturated with CO. This result suggests that the saturated CO adsorption blocked the active sites for methanol dissociation, which led to an inhibition of the dissociation. As the amount of CO adsorption decreased, the intensities of the major CO peaks at approximately 2054 and 2076 cm^{-1} (L_1 and L_2 CO) diminished. The decomposition of methanol gradually yielded the L_2 CO at 2076 cm^{-1} and the carbonyl species at 1715 cm^{-1} (Figure 12B). However, Figure 10 clearly indicates that the CO adsorbed on the Pt/SBA-15(-COOH) surface could have a high population on the L_3 sites, as indicated by the intensity of the peak at 2094 cm^{-1}; however, the CO generated by the decomposition of methanol did not occupy the L_3 sites (2094 cm^{-1}) in this study. Therefore, the L_3 sites were strongly associated with methanol dissociation. In contrast, the results of identical experiments shown in Figure S5 were also compared to the spectrum of Pt/SBA-15; the CO bound to the L_1 and L_2 sites was found to inhibit the decomposition of the adsorbed methanol, irrespective of the level of CO coverage on the Pt surface. These results imply that the decomposition of methanol occurred primarily on the L_1 and L_2 sites.

Nanoscale Accepted Manuscript

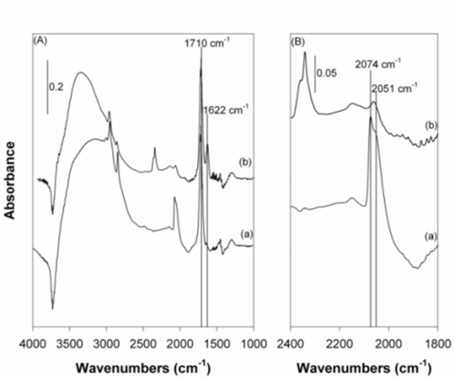

Fig. 11 Time dependence of the IR spectra for the co-adsorption of methanol and air onto the 2.526% Pt/SBA-15(-COOH) at 298 K with (a) the injection of 5 μL of CH_3OH onto the catalyst for 5 min and with (b) 30 mL/min airflow passed through the methanol pre-covered catalyst for 3 min.

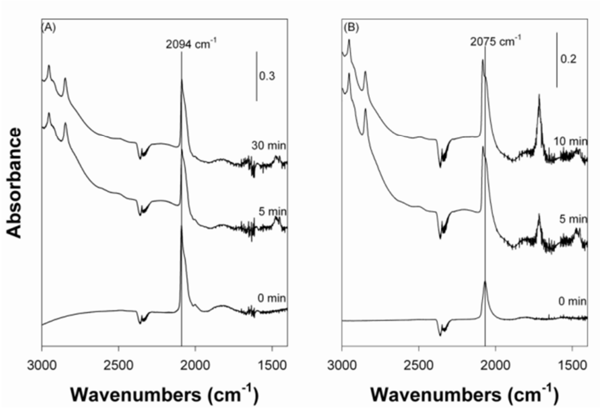

Fig. 12 Time-dependent IR spectra for a 5 μL injection of CH_3OH onto pure CO pre-covered 2.52% Pt/SBA-15(-COOH): (A) 20 min of CO exposure; (B) 30 s of CO exposure.

4. Discussion

The TEM images in Figure 3 revealed that the long, spheroidal Pt NPs formed in the channels of pure SBA-15, where the ends of the spheroids were terminated by {111} facets, and the side surfaces were bounded by {100} facets. The five-fold twinned surfaces were observed in the top-view HRTEM image. The shapes of the Pt nanocrystals depended on the number and type of twin planes in the seed crystals. Previous reports have mentioned that multiple twinned seeds can evolve into five-fold twinned rods.[37] The order of the surface energies is (110) > (100) > (111) for the fcc Pt structure.[7] Therefore, the shape of a metal nanostructure is usually determined by the minimization of surface energy. A mixture of both {111} and {100} facets can minimize the total surface energy. However, growth along the closed- packed {111} direction has priority based on the lowest energy principle.[18] The morphology of fcc metals may strongly depend on the growth rate along their [100] and [111] directions.[18] Based on the anisotropic growth, the single crystal seeds could become cuboctahedral and continue to develop to form rod structures when the ratio of growth rates along the {100} and {111} axes is slightly less than 1.[37] When the growth rate of {100} is larger than that of {111}, the crystal structure may prefer to form an octahedral shape.[37] The Pt NPs with octahedral shapes could form outside of the channels of pure SBA-15 support because the ratio of (100)/(111) for the growth rate was greater than 1. However, the long spheroid-like Pt NPs in the channels of pure SBA-15 might follow the growth mechanism of nanorod structures. The shape of the Pt nanostructures that was formed on pure SBA-15 materials might be associated with the difference in the growth rates between the {100} and {111} axes. The channels of SBA-15 restricted the growth of Pt along the <100> direction and enhanced the Pt NP aggregation along the <111> direction, which induced the formation of spheroid-like or rod-like Pt NPs. The extra strain energy for five-fold twinned seeds with (111) planes may maximize the surface coverage with (111) facets and minimize the lowest surface energy.

The XRD spectra in Figures 8 have illustrated that the $(H_3O_2)PtCl_6$ species were difficult to form on SBA-15(-COOH), as the Pt^{4+} deposited. It implied that the carboxylic acid groups on SBA-15 might strongly interact with the Pt^{4+} ions. However, the presence of carboxylic acid groups on SBA-15 may induce the formation of nearly spherical Pt NPs. The multi-twinned Pt crystals were not present on the SBA-15(-COOH) support. Previous reports have indicated that colloidal stabilizers, such as poly(vinyl pyrrolidone) (PVP) or poly(acrylic aid) (PAA), that are used as capping agents can effectively control the shape of Pt NPs.[14-19] The temperature-dependent IR spectra of the Pt^{4+} loaded on SBA-15 with –COOH groups that were measured in an air stream are shown in Figure 13. The intensities of the characteristic peaks for the –COOH functionalized SBA-15 support that appeared at 2909-3001 cm^{-1} for the ν(C-H) and at 1768 cm^{-1} for the ν(C=O) of the carboxylic acid groups could be enhanced with increased calcination temperature. However, adsorbed CO and CO_2 were gradually generated at temperatures greater than 523 K by the dissociation of the carboxylic acid groups. The in situ IR spectra of Pt^{4+}/SBA-15(-COOH) in air streams showed that the carboxylic acid groups could not be completely removed via calcination and reduction at 673 K.

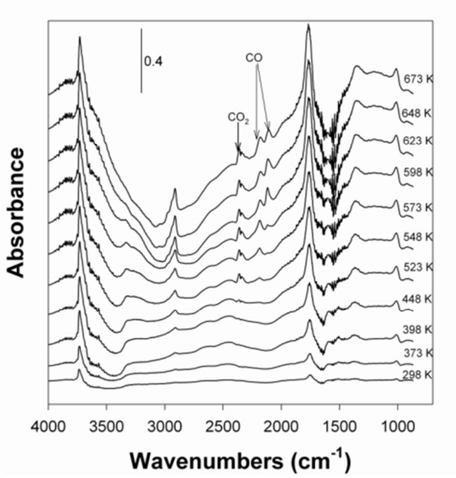

Nanoscale Accepted Manuscript

Figure 13 Temperature-dependent IR spectra of SBA-15(-COOH) that was impregnated with 2.52% Pt^{4+} under an air stream

To evaluate the incorporation efficiency of the -COOH group, the total acidic capacity of SBA-15(-COOH) samples undergoing calcination and Pt^{4+} impregnation were determined by potentiometric titration with an aqueous solution of NaOH (0.01 M). The results are presented in Table S1. It can be realized from the data that the acidic capacity of SBA-15(-COOH) decreased from 1.04 mmol H^+/g to 0.52 mmol H^+/g after calcination treatment. When Pt^{4+} impregnated on SBA-15(-COOH), the acidic capacity decreased to 0.27 mmol H^+/g. The calcination treatment of Pt^{4+}/ SBA-15(-COOH) merely led to the value slightly decreased to 0.25 mmol H^+/g. When Pt^{4+} was impregnated on the SBA-15(-COOH) through calcination treatment, the acidic capacity still could remain at 0.19 mmol H^+/g. Therefore, the residual carboxylic acid on SBA-15 might play the role of capping agent to control the shape of the Pt NPs. The carboxylic acid groups might have strong interactions with the (111) facet, which might result in inhibition of (111) facet growth and the formation of nearly spherical Pt NPs.

Using XAS measurements, we determined that the Pt^{4+} impregnated in SBA-15(-COOH) could be directly transformed to metallic Pt^0 NPs in air and in N_2 environments at temperatures greater than 623 K. However, there is no reported literature regarding Pt^{4+} ions on oxide supports that are directly transformed into metallic Pt via calcination treatments in air. This phenomenon might depend on the SBA-15 functionalized with carboxylic acid groups. Figure S6A shows the DR-UV–Vis spectra of SBA-15 impregnated with H_2PtCl_6 with and without the reduction treatments. The Pt(IV) species on SBA-15 produced a broad absorption band at 230-430 nm (Figure S6A-a). After the impregnated Pt^{4+}/SBA-15 sample was thermally treated under CO gas, the characteristic absorption peak of Pt(IV) almost disappeared (Figure S6A-b). The spectrum of the Pt/SBA-15 sample that was reduced through H_2 treatment is shown in Figure S6A-c and is similar to spectrum (b). The temperature-dependent in situ L_3-edge XANES spectra of Pt^{4+} impregnated on SBA-15 in a 5% CO stream are shown in Figure S6B. These spectra reveal that the white-line intensity of the Pt species is apparently diminished at temperatures greater than 473 K. These results imply that the Pt^{4+} species could be reduced when CO species were present. The IR spectra in Figure 10 clearly demonstrate that gaseous CO could be formed over the course of the calcination process for Pt^{4+}/SBA-15(-COOH). Figure 14 presents the temperature-programmed desorption (TPD) spectra of as-impregnated Pt^{4+}/SBA-15(-COOH) in a He stream; CO (28 amu) and CO_2 (44 amu) were monitored by QMS during the course of the TPD process. The formation of CO and CO_2 could be ascribed to dissociation of carboxylic acid groups on SBA-15. It was noteworthy that large amount of CO could desorb at wide temperature range (400-850 K). These results therefore suggest that the transformation of Pt^{4+} on SBA-15(-COOH) to metallic Pt^0 NPs might be caused by the generation of a CO reductant, which may be derived from the dissociation of carboxylic acid groups. Kang et al. have reported the synthesis of Pt nanocubes using CO as a reducing agent, which was generated via the dehydration of formic acid.[38] The large difference in catalytic activity of methanol oxidation between Pt/SBA-15(-COOH) and Pt/SBA-15 was proposed to depend on the shape of Pt NPs on both supports. The near-spherical Pt NPs formed on SBA-15(-COOH) support apparently provided higher efficiency of methanol oxidation than the spheroidal Pt NPs on SBA-15.

According to the literature, the lower frequency bands at ~2075 and 2054 cm^{-1} in the IR spectra of CO adsorbed onto Pt surfaces correspond to CO on defect sites, such as edges and kinks.[39-43] The band located at 2096 cm^{-1}can be assigned to CO adsorbed onto the close-packed terrace sites or onto oxidized $Pt^{\delta+}$ atoms.[43] The IR spectra of the CO and methanol co-adsorbed onto the Pt/SBA-15 and Pt/SBA-15(-COOH) catalysts in Figures 12 and S5 enabled the sites for methanol dissociation to be identified. On the Pt/SBA-15(-COOH) catalyst, the saturated CO adsorption blocked all active sites, which completely inhibited the methanol dissociation; however, a decreasing in the amount of CO adsorption resulted in only the loss of intensity in the IR peak at 2094 cm^{-1} and could therefore trigger the decomposition reaction. The adsorbed methanol might dissociate on terrace sites (L_3 sites). However, the sites for the methanol decomposition on Pt/SBA-15 may be the defect sites (L_1 and L_2 sites). Our experimental results indicated that the CO intermediate that was generated from methanol that was decomposed on the terrace sites of Pt/SBA-15(-COOH) can be rapidly oxidized by air at room temperature (Figure 11). However, the IR spectra of the CO that was adsorbed onto the Pt NPs on the SBA-15(-COOH) indicated that numerous terrace sites were present on the Pt surface and that the terrace sites were more active than the defects sites for methanol decomposition. The large quantity of terrace sites (L_3 sites) that were formed on the Pt/SBA-15(-COOH) increased the efficiency of the methanol dissociation and enhanced the activity of the methanol oxidation.

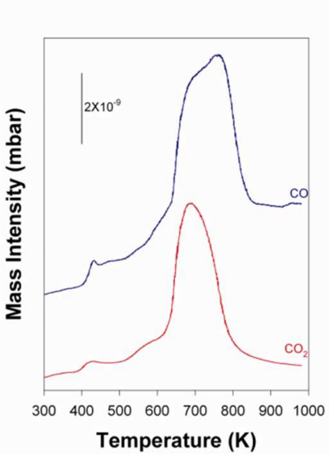

Figure 14 Temperature-programmed desorption spectra of 2.52 % Pt^{4+}/SBA-15(-COOH) in He stream

5. Conclusions

Nanoscale Accepted Manuscript

In this paper, the mechanism and characterization of Pt NPs generated on SBA-15 and SBA-15(-COOH) are investigated in detail. We have demonstrated that SBA-15 can effectively control the shape of Pt NPs through an impregnation process and subsequent thermal treatment. In the channels of pure SBA-15, long, spheroidal Pt NPs can be formed via the growth mechanism of a nanorod structure. The channels of the SBA-15 restricted the growth of Pt along the <100> direction and enhanced the Pt NP aggregation along the <111> direction, which induced the formation of spheroid-like or rod-like Pt NPs. However, the carboxylic acid functionalization of SBA-15 can cause the Pt NPs to form near-spherical shapes. The Pt4+ species on SBA-15(-COOH) can be directly transformed to metallic Pt0 NPs through calcination treatments in air or N2 streams because the generation of the CO reductant is derived from the dissociated carboxylic acid groups. The methanol oxidation activity on a Pt surface is strongly dependent on shape of Pt particles. The near-spherical Pt NPs on the SBA-15(-COOH) exhibited higher catalytic activity during methanol oxidation than did the rod-like Pt NPs on the pure SBA-15. The near-spherical Pt particles on the SBA-15(-COOH) contained large numbers of terrace sites on their surfaces, which led to high efficiency during methanol oxidation.

Acknowledgements

The financial support from the National Science Council of the Republic of China (NSC 100-2113-M-182-001-MY3) and Chang-Gung Memorial Hospital (CMRPD5C0021) is gratefully acknowledged. We are also grateful for access to the in situ X-ray absorption spectroscopy (BL17C1) results collected at the National Synchrotron Radiation Research Center (NSRRC).

Notes and references

[a] Center for General Education, Chang Gung University, 259 Wen-Hwa 1st Road, Kwei-Shan Tao-Yuan, Taiwan, 333, Republic of China
[b] Department of Pathology, Chang Gung Memorial Hospital, 5 Fusing St., Kwei-Shan Tao-Yuan, Taiwan, 333, Republic of China
[c] Graduate Institute of Applied Science and Technology, National Taiwan University of Science and Technology,43 Keelung Road, Sec. 4, Taipei 106, Taiwan, Republic of China
[d] National Synchrotron Radiation Research Center Hsinchu 300, Taiwan, Republic of China
[e] Department of Material Science and Engineering, National Tsing Hua University, Hsinchu 300, Taiwan, Republic of China
[f] Department of Chemistry, National Central University, Chung-Li, Taiwan 320, Republic of China

Electronic Supplementary Information (ESI) available: Total acidity capacity of SBA-15(-COOH) and Pt^{4+}/SBA-15(-COOH); Pore size distributions of SBA-15 and SBA-15(-COOH); TEM images of Pt NPs on SBA-15 and on SBA-15(-COOH); Time-dependent IR spectra of the co-adsorption of CH$_3$OH and air onto Pt/SBA-15; Time-dependent IR spectra for a 5 μL injection of CH$_3$OH onto pure CO pre-covered Pt/SBA-15; UV–Vis diffuse reflectance spectra of Pt/SBA-15; Pt L-edge XANES spectra of Pt^{4+}/SBA-15 in CO stream at different temperatures.

1 J. Zhu, T. Wang, X. Xu, P. Xiao and J. Li, Appl. Catal. B, 2013, 130, 197.
2 Z. Jiang, Y. Yang, W. Shangguan and Z. Jiang, J. Phys. Chem. C, 2012, 116, 19396.
3 M.F. Williams, B. Fonfé, A. Jentys, C. Breitkopf, J.A.R. van Veen and J.A. Lercher, J. Phys. Chem. C, 2010, 114, 14532.
4 T. Ebashi, Y. Ishida, Y. Nakagawa, S. Ito, T. Kubota and K. Tomishige, J. Phys. Chem. C, 2010, 114, 6518.
5 J. Zhu, K. Kailasam, X. Xie, R. Schomaecker and A. Thomas, Chem. Mater., 2011, 23, 2062.
6 V.T.T. Ho, C.J. Pan, J. Rick, W.N. Su and B.J. Hwang, J. Am. Chem. Soc., 2011, 133, 11716.
7 Y.B. He, G.R. Li, Z.L. Wang, Y.N. Ou and Y.X. Tong, J. Phys. Chem. C, 2010, 114, 19175.
8 T.H.M. Housmans and M.T.M. Koper, J. Phys. Chem. B, 2003, 107, 8557.
9 M. Rodríguez-López, J. Solla-Gullón, E. Herrero, P. Tuñón, J.M. Feliu, A. Aldaz and Jr. Carrasquillo, J. Am. Chem. Soc., 2010, 132, 2233.
10 S.W. Lee, S. Chen, W. Sheng, N. Yabuuchi, Y.T. Kim, T. Mitani, E. Vescovo and Y. Shao-Horn, J. Am. Chem. Soc., 2009, 131, 15669.
11 C. Li, M. Imura, and Y. Yamauchi, Chem. Eur. J. 2014, 20, 3277.
12 C. Li, T. Sato and Y. Yamauchi, Angew. Chem. Int. Ed. 2013, 52, 8050.
13 Y. Yamauchi, J. Ceram. Soc. Jpn., 2013, 121, 831.
14 M. Noġami, R. Koike, R. Jalem, G. Kawamura, Y. Yang and Y. Sasaki, J. Phys. Chem. Lett., 2010, 1, 568.
15 R. Narayanan and M.A. El-Sayed, Nano lett., 2004, 4, 1343.
16 T.S. Ahmadi, Z.L. Wang, T.C. Green, A. Henglein and M.A. El-Sayed, Science , 1996, 272, 1924.
17 L. Qu, L. Dai and E. Osawa, J. Am. Chem. Soc., 2006, 128, 5523.
18 B. Qiao, A. Wang, X. Yang, L.F. Allard, Z. Jiang, Y. Cui, J. Liu, J. Li and T. Zhang, Nature Chem., 2011, 3, 634.
19 Y. Wu, S. Cai, D. Wang, W. He, Y. Li, J. Am. Soc. Chem., 2012, 134, 8975.
20 H. Berndt, A. Martin, A. Brückner, E. Schreier, D. Muller, H. Kosslick, G.U. Wolf and B. Lücke, J. Catal., 2000, 191, 384.
21 V. Fornés, C. López, H.H. López and A. Marťinez, Appl. Catal. A 2003, 249, 345.
22 M. Baltes, K. Cassiers, P. Van Der Voort, B.M. Weckhuysen, R.A. Schoonheydt and E.F. Vansant, J. Catal., 2001, 197, 160.
23 G. Du, S. Lim, M. Pinault, C. Wang, F. Fang, L. Pfefferle and G.L. Haller, J. Catal., 2008, 253, 74.
24 C.H. Tu, A.Q. Wang, M.Y. Zheng, X.D. Wang and T. Zhang, Appl. Catal. A, 2006, 297, 40.
25 K. Yoshida, C.G. Arellano, R. Luque and P.L. Gai, Appl. Catal. A, 2010, 379, 38.
26 C.M. Chanquía, K. Sapag, E. Rodríguez-Castellón, E.R. Herrero and G.A. Eimer, J. Phys. Chem. C, 2010, 114, 1481.
27 A.K. Prashar, R.P. Hodgkins, J.N. Chandran, P.R. Rajamohanan and R. N. Devi, Chem. Mater., 2010, 22, 1633.
28 H. Wang, H. Y. Jeong, M. Imura, L. Wang, L. Radhakrishnan, N. Fujita, T. Castle, O. Terasaki, and Y. Yamauchi, J. Am. Chem. Soc. 2011, 133, 14526.
29 P. Karthika, H. Ataee-Esfahani, H.Wang, M. A. Francis, H. Abe, N. Rajalakshmi, K. S. Dhathathreyan, D. Arivuoli, and Y. Yamauchi, Chem. Asian J. 2013, 8, 902.
30 H. Wang, M. Imura, Y. Nemoto, S.E. Park, and Y. Yamauchi, Chem. Asian J. 2012, 7, 802.

Nanoscale Accepted Manuscript

31 J.L. Gu, J.L. Shi, G.J. You, L.M. Xiong, S.X. Qian, Z.L. Hua and H.R. Chen, Adv. Mater. 2005, 17, 557.

32 L. Shang, T. Bian, B. Zhang, D. Zhang, Li.Z. Wu, Chen.H. Tung, Y. Yin and T. Zhang, Angew. Chem. Int. Ed. 2014, 53, 250.

33 J. R. Deka, H.M. Kao, S.Y. Huang, W.C. Chang, C.C. Ting, P. C. Rath and C.S. Chen, Chem. Eur. J. 2014, 20, 894.

34 C.S. Chen, Y. T. Lai, T. W. Lai, J. H. Wu, C. H. Chen, J. F. Lee and H. M. Kao, ACS Catal., 2013, 3, 667.

35 F. Bernardi, M.C.M. Alves and J. Morais, J. Phys. Chem. C, 2010, 114, 21434.

36 B.R. Cuenya, J.R. Croy, S. Mostafa, F. Behafarid, L. Li, Z. Zhang, J.C. Yang, Q. Wang and A.I. Frenkel, S J. Am. Chem. Soc., 2010, 132, 8747.

37 Y. Xiong and Y. Xia, Adv. Mater., 2007, 19, 3385.

38 Y. Kang, X.C. Ye and C.B. Murray, Angew. Chem. Int. Ed., 2010, 49,6156.

39 C. Daniel, M.O. Clarté, S.-P. Teh, O. Thinon, H. Provendier, A.C. Van Veen, B.J. Beccard, Y. Schuurman and C. Mirodatos, J. Catal., 2010, 272, 55.

40 S.D. Ebbesen, B.L. Mojet and L. Lefferts, J. Catal., 2007, 246, 66.

41 M.J. Lundwall, S.M. McClure and D.W. Goodman, J. Phys. Chem. C, 2010, 114, 7904.

42 H. Song, R.M. Rioux, J.D. Hoefelmeyer, R. Komor, K. Niesz, M. Grass, P. Yang and G.A. Somorjai, J. Am. Chem. Soc., 2006, 128, 3027.

43 P. Bazin, O. Saur, J.C. Lavalley and M. Daturi, Phys. Chem. Chem. Phys., 2005, 7, 187.

Nanoscale Accepted Manuscript

This journal is © The Royal Society of Chemistry 2012